Journal of Fluids and Structures (2001) **15,** 59–81
doi:10.1006/jfls.2000.0327, available online at http://www.idealibrary.com on IDEAL®

SELF-SUSTAINED OSCILLATION OF A SUBMERGED JET IN A THIN RECTANGULAR CAVITY

N. J. Lawson

Department of Aerospace, Power and Sensors, Royal Military College of Science, Cranfield University, Shrivenham, Wiltshire, SN6 8LA, U.K.

AND

M. R. Davidson

G.K. Williams Cooperative Research Centre for Extractive Metallurgy, Department of Chemical Engineering, The University of Melbourne Parkville, Vic. 3052, Australia

(Received 12 August 1999, and in final form 24 June 2000)

Self-sustained oscillating jet flow of water in a rectangular cavity, having thickness which is small relative to its width, is measured using LDA and PIV, and predicted using a transient two-dimensional computational fluid dynamic model which incorporates a resistance coefficient for cross-flow. The basic geometry represents a scale model of a mould typical of thin slab steel casting. The frequency of the oscillation was found to be independent of cavity thickness. It also increased as the cavity width decreased down to some critical value, after which the oscillation ceased. The frequency was observed to increase with nozzle diameter and was found to decrease with increasing length/width ratio of the cavity. The numerical model, with a fixed dimensionless cross-flow resistance coefficient, was shown to predict the Strouhal number of the oscillation and the dimensionless mean velocity profiles in the jet extremely well.

1. INTRODUCTION

In continuous slab casting, liquid metal is injected into a water-cooled mould as two lateral jets through a submerged entry nozzle (SEN). As the outer edges of the metal cool, they solidify, forming a solid shell which increases in thickness as it descends in the mould. The technique is now a well-established method for producing steel for various applications (Nilles & Etienne 1991). The process includes turbulent liquid flow in the SEN and in the mould, heat transfer, and solidification. Considerable effort has been devoted to describing this coupled, three-dimensional system in studies ranging from the implementation of combined models [e.g. Huang *et al.* (1992), Seyedein & Hasan (1997)] to those focusing on flow specific aspects in the nozzle (Najjar *et al.* 1995) and in the mould (Thomas *et al.* 1990). Austin (1992) has surveyed the literature on the modelling of continuous casting, and Herbertson *et al.* (1991) reviewed the use of mathematical and water modelling studies to optimize performance. Samarasekera *et al.* (1997) discussed the modelling of both past and new developments in the technology.

Casting slabs which are closer to the desired thickness can improve the efficiency of the process by reducing the cost of subsequent hot rolling (Honeyands & Herbertson 1995). However, for thin slab casting to achieve the same throughput as conventional continuous

0889–9746/01/010059 + 23 $35.00/0

casting, the casting speeds must be higher. This results in free-surface oscillations of the liquid metal in the mould which can lead to poor cast surface finish and flux entrainments leading to lower product quality (Honeyands *et al.* 1992; Honeyands 1994). Similar problems occur in strip casting of aluminium (Espedal *et al.* 1993). Understanding the fluid dynamics in the mould is necessary to minimize these limitations at increased casting rates, and to study the effect of the oscillations on superheat dissipation and uniformity of shell growth.

Studies with water models of thin slab caster moulds (Gupta & Lahiri 1994; Honeyands 1994) show that the observed surface disturbances at increased casting rates can result from an unstable flow pattern associated with confined jet oscillation. The jets emanating from the SEN can oscillate across the broad face of the mould. Honeyands (1994) concluded that the jet oscillation is similar to that which occurs in a blind cavity (Molloy 1969). The flow oscillation occurs in the presence of a steady flow through the nozzle and is thus not being driven by unsteadiness in the delivery system. The oscillation of a confined jet is an example (Villermaux & Hopfinger 1994; Maurel *et al.* 1996) of that which can occur when a shear layer is bounded by a recirculation zone (Rockwell 1983). The confined jet in a fluidic oscillator (Viets 1975; Shakouchi 1989; Morris *et al.* 1992) is a related example. Such oscillations are of lower frequency, and are less well studied, than those driven by the inherent instability of a shear layer (Rockwell 1983; Rockwell & Naudascher 1979).

Self-sustaining oscillations of a confined jet rely on the existence of a feedback loop linking each side of the jet. For a thin slab caster mould, feedback occurs via a cross-flow through the gap between the nozzle shaft and the broad face of the mould wall. The schematic in Figure 1 shows the main features of the flow from an idealized nozzle consisting of a simple pipe. It shows the two recirculation cells on either side of the jet, and the cross-flow. As the jet oscillates, the recirculation cells move up and down and the cross-flow oscillates in response.

Honeyands was able to predict sustained oscillation in a computational model based on a simplified system consisting of a single jet into a blind cavity with free outflow conditions at the top. More recently, Gebert *et al.* (1998*a*, *b*) have numerically predicted single-jet oscillation of the flow sketched in Figure 1 using a two-dimensional mould geometry with outflow at the bottom. However, they made no quantitative comparisons with experiment. Indeed, the primary factor limiting further development of computational models of the oscillation has been the lack of detailed measurements of the fluctuating flow field. Laser doppler anemometry (LDA) (Durst *et al.* 1981) and particle image velocimetry (PIV) (Pickering & Halliwell 1985; Adrian 1991) are two nonintrusive velocity measurement techniques which can provide significantly greater quantities of velocity data than is currently available.

Recently, the present authors have used LDA and PIV techniques (Lawson & Davidson 1998*a*, *b*, 1999) to measure oscillatory characteristics in a water model for the single-jet flow represented in Figure 1. The authors measured the response of the cross-flow oscillation to changes in casting rate, nozzle wall thickness, and nozzle submergence. The aim of the present paper is to extend that work to study the oscillating jet flow throughout the whole cavity, and to use these data to validate a numerical flow model based on that of Gebert *et al.* (1998*a*, *b*).

2. PHYSICAL MODELLING

2.1. Experimental Rig

The experimental rig consisted of a mould, a tundish (header tank) and an outlet manifold as shown in Figure 2. A glass-walled mould was used to ensure good optical access for the

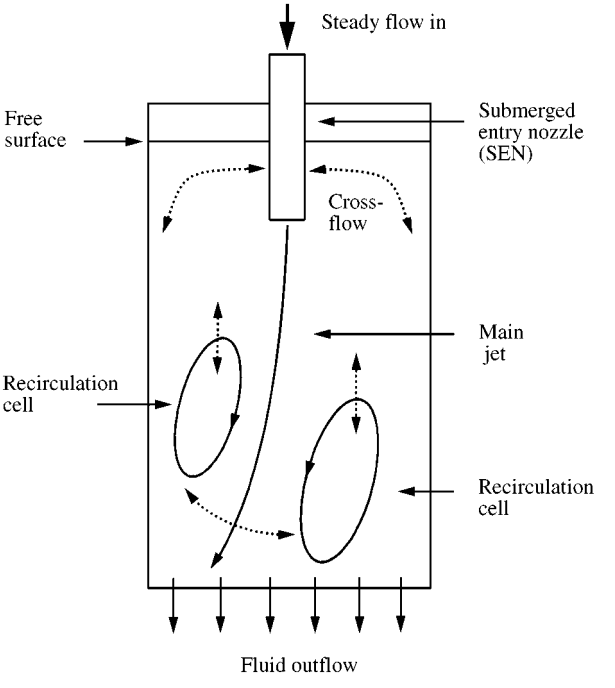

Figure 1. Schematic of the oscillating jet flow field.

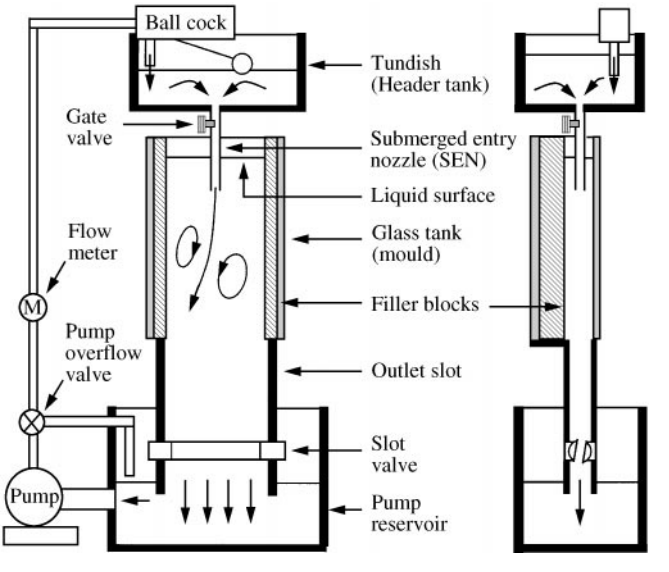

Figure 2. Schematic of the experimental rig.

LDA and PIV measurement systems. With reference to Figure 3(b) and 3(c), the mould had maximum dimensions of length $L = 800$ mm, width $W = 500$ mm and thickness $H = 180$ mm. These sizes allowed a wide range of mould geometries to be tested including a 1/3 scale of the (full-scale) mould geometry considered by Honeyands (1994). Mould width and thickness was varied by inserting polystyrene and perspex filler blocks into the mould

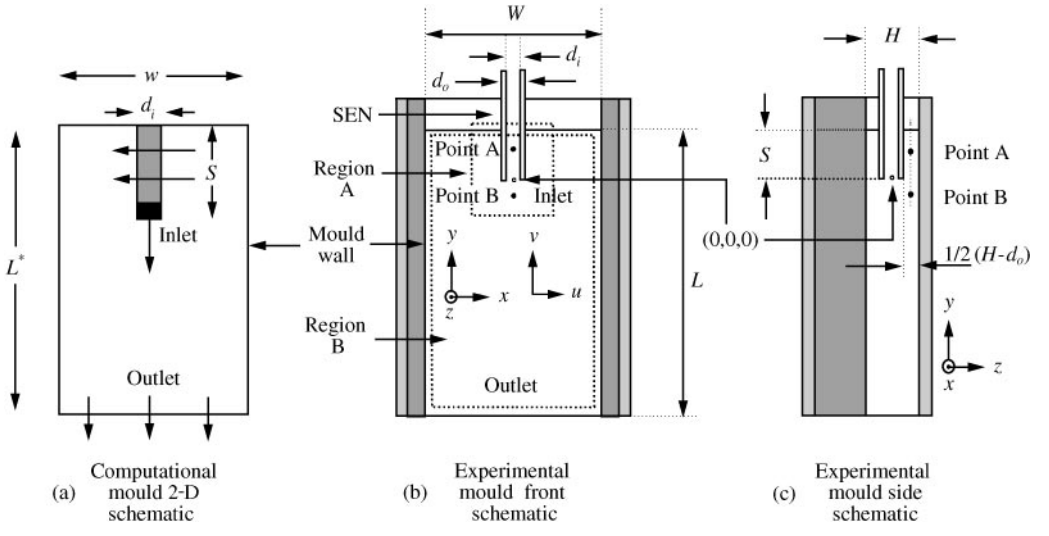

Figure 3. Schematic showing (a) computational parameters and (b), (c) experimental parameters. In (a) the black square defines the inlet and the grey area represents the region of the SEN in which a resistance to cross-flow is set. The length ($L^* = 1050$ mm) extends from the liquid surface to the slot valve at the bottom of the manifold. W = Mould width, L = mould length, L^* = dimensionless length, H = mould thickness, d_o = SEN outer diameter, d_i = SEN inner diameter, S = SEN submergence.

and clamping them onto the inside of the walls. These blocks allowed a range of widths from 80 mm $< W <$ 500 mm and thickness from between 55 mm $< H <$ 180 mm.

A 200 l tundish (header tank) mounted 500 mm above the mould supplied water with a constant head to the mould through a SEN. For all the measurements the SEN was chosen to be a simple pipe producing a single jet at its exit. (A bifurcated nozzle with twin lateral jet flows, characteristic of industrial practice, will be the subject of a subsequent paper). A glass SEN (internal diameter $d_i = 33$ mm) and a set of PVC SENs (internal diameters in the range 18 mm $< d_i <$ 38 mm) were used. SEN wall thicknesses were 2·5 mm for the glass nozzle and 1–2 mm for the PVC nozzles.

The bottom of the mould was fitted with a 300 mm $\times$ 500 mm $\times$ 100 mm outlet manifold containing an adjustable slot valve for flow control (see Figure 2). The manifold design was found to be critical for ensuring that the oscillation was not biased by the outflow condition, and a number of configurations were tried before obtaining reliable jet oscillations. Lawson & Davidson (1999) discuss this in more detail. The final choice of manifold, based on an outlet slot and slot valve, ensured an even outflow across the mould width and was found to provide reliable oscillations for the complete range of mass flows tested. It was also found necessary to add a 250 mm $\times$ 500 mm $\times$ 100 mm extension slot to the bottom of the manifold to prevent air entrainment from the pump reservoir.

Water was supplied to the tundish from a Harland 2 kW centrifugal pump. An overflow was fitted onto the pump outlet to prevent the pump stalling at lower rates and simply bypassed water back into the pump reservoir. The flow rate into the tundish was controlled by a commercially available Apex ballcock with a 150 mm diameter float. This ensured a constant head was maintained in the tundish for a given flow rate through the mould. The flow through the SEN was controlled by a gate valve placed at the tundish outlet. With this system, any selection of flow rate required a number of minutes to stabilize, but reliable flow

control could be achieved for a range of casting rates of between 0·5 and 2·0 m/min. Here "casting rate" refers to the mean discharge velocity from the manifold.

The instrumentation on the rig was simply a Coles Palmer electronic turbine flowmeter, model 05610-40. This was used to monitor the casting rate and was placed 250 mm from the pump overflow valve and calibrated. The calibration procedure consisted of measuring the time taken for the water level in the mould to fall 50 mm for a range of flow meter readings. With the known distance and time, the casting rate in m/min could then be estimated.

2.2. Measurement Systems

Two measurement systems were chosen to analyse the flow field in the mould. These were LDA for pointwise analysis and PIV for full field flow analysis. The high sampling rate of the LDA system allowed detailed temporal analysis of the flow to obtain the oscillatory properties of the jet while the PIV allowed analysis of flow structures in the mould.

2.2.1. LDA system

Two-dimensional (2-D) LDA measurements were made using a Dantec FibreFlow system and a 58N40 FVA covariance signal processor as illustrated in Figure 4. The back-scatter probe was set-up to use the green line (514·5 nm) for the horizontal velocity component u and the blue line (488 nm) for the vertical velocity component v from a Coherent 4 W argon ion laser. The FibreFlow system included a Bragg cell to provide a 40 MHz frequency shift for directional discrimination on both components. Bandwidths chosen varied from

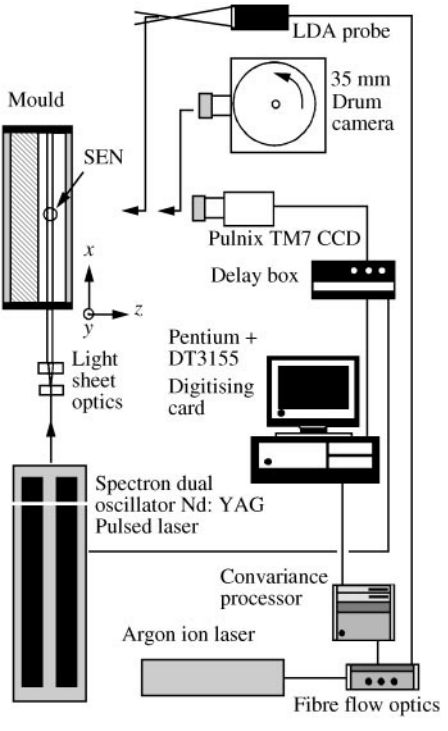

Figure 4. Schematic of the LDA and PIV experimental setup.

0·12 MHz (± 0·06 MHz) to 1·2 MHz (± 0·6 MHz) depending on whether cross-flow or jet measurements were being taken. This corresponded to flow velocity ranges of ± 200 mm/s to ± 2 m/s with a focal length of 250 mm and fringe spacing of 3·395 μm. A focal length of 250 mm was chosen to give sufficient spatial resolution in the mould and corresponded to a measurement volume of 0·117 mm × 0·117 mm × 1·544 mm for the horizontal velocity component u and of 0·111 mm × 0·111 mm × 1·464 mm for the vertical velocity component v. The fluid was seeded with Fidene silver-coated hollow glass spheres with a size range of 10–30 μm and a specific gravity of 1·1 to adequately follow the flow (Dring 1982). Sampling periods of 200–300 s were used for each data point. Seeding and laser power levels were adjusted before acquisition to ensure an average data rate of around 100 Hz over the sampling period. This ensured adequate temporal resolution for the expected oscillatory frequencies and the raw data was subsequently resampled for the spectral analysis as outlined previously (Lawson & Davidson 1999).

2.2.2. PIV system

The PIV imaging system was based on a commercially available Pulnix CCD and an in-house developed 35 mm drum camera (Lawson & Liow 1998). In both cases, a Spectron dual SL800 Nd:YAG pulsed laser was used as a light source as shown in Figure 4. The SL800 at maximum power outputs a collinear beam of two 450 mJ pulses of 532 nm light at 12·5 Hz with pulse durations of 5 ns and pulse separations variable from 1 μs to 40 ms. For the flows measured here a pulse separation of between 3 and 10 ms was chosen and the output beam was expanded into a collimated light sheet by using a plano concave and plano cylindrical lens arrangement. For the CCD system, synchronization with the laser was achieved by using the video signal and a delay box to drive the laser flash lamp power supplies at 12·5 Hz. Data from the CCD was directly digitized into 768 × 576 pixel images at up to 4 Hz by using a data translation DT3155 digitizing board. Sequences of up to 80 frames were stored to analyse cycles of the flow.

For the drum camera, the shutter was simply open for a given oscillation cycle and images exposed at 2 Hz onto TMAX400 film mounted onto the drum which was subsequently push processed to 800ASA. The camera can store up to 75 half-frame images on any given run with a resolution of 1600 × 2400 pixels per image. For this reason the drum camera was used to look at the full flow field in the mould, shown as region B in Figure 3(b), while the CCD was restricted to the smaller cross-flow region, shown as region A in Figure 3(b).

The digitized frames were processed into velocity data by using dual-field cross-correlation and image shifting autocorrelation software written by the first author. These techniques have been described by Lecordier *et al.* (1994) and Adrian (1986), respectively. An interrogation region resolution of 64 × 64 and 128 × 128 was used with a 50% overlap to yield 450 and 2000 vector points per image for the CCD and drum camera system, respectively. The imaging area varied from 200 mm × 150 mm when analysing the cross-flow region to 500 mm × 800 mm when recording the full flow field. With a grid of 25 × 18 and 36 × 53 vectors these two imaging areas corresponded to spatial resolutions of 8.3 and 15·1 mm and full-scale measurement ranges of ± 0·2 and ± 2·2 m/s, respectively. Following the initial processing, a validation range based on one-third of the two measurement ranges was used to remove erroneous vectors (Keane & Adrian 1992; Lawson *et al.* 1997). Any missing data points were then inerpolated and smoothed using algorithms described by Landreth & Adrian (1988). In this case, a smoothing radius of 1–3 interrogation regions was chosen to match the spatial scales in the majority of the flow.

2.3. Flow Measurements

The characterization of the oscillatory jet involved recording LDA and PIV data in both the cross-flow region and the main body of the jet. For the LDA measurements in the cross-flow region, two points (A and B) were chosen as shown in Figure 3(b) and 3(c). An analysis of the velocity time series at the two data points allowed the oscillation frequency, the r.m.s. cross-flow velocity, and the cycle-averaged peak velocity to be determined. Only r.m.s. and cycle-averaged peak velocity of the cross-flow was considered here due to the sinusoidal nature of the cross-flow, which had near zero mean values. LDA measurements in the jet below the SEN were also taken in the central vertical plane ($z = 0$) along the (vertical) y-axis and along a (horizontal) x-traverse at $y = -32$ mm; both mean and r.m.s. vertical velocity were measured.

Point A was positioned on the centre-line of the broad face of the mould ($x = 0$) and vertically at a mid-point between the free surface and the SEN exit. In the transverse (z) direction, point A is notionally located midway between the SEN and the mould wall, but for gap widths less than 10 mm, this position was determined by a z-traverse to coincide with the maximum in the transverse velocity profile. Point B was fixed at $x = 0$, $y = -33{\cdot}0$ mm, $z = 29{\cdot}5$ mm. This location was chosen to ensure a valid measurement of the additional cross-flow past the jet below the SEN exit, as discussed by Lawson & Davidson (1999).

The PIV measurements were considered in the two areas, Regions A and B, as shown in Figure 3(b). Region A was used to study spatial flow structures in the cross-flow region, upto the free surface and just below the SEN exit. Region B was used to study spatial flow structures in the plane of the jet across the complete mould area. Although temporal evolution of these structures could also be examined, the PIV was not used to analyse jet oscillation frequencies since sampling rates were only a maximum of 4 Hz while the LDA provided data with average sampling rate of around 100 Hz over the sampling period.

Measurements were taken for selected values of the mould width (W), the mould thickness (H), the inner diameter of the SEN (d_i), and the mean liquid velocity at the SEN exit (V_{in}). Data showing the effect of changing the SEN submergence (S) and the nozzle wall thickness (by increasing the SEN outer diameter d_o) is presented in previous papers (Lawson & Davidson 1998*a*, *b*, 1999), and consequently is not described here. Tables 1 and 2 list the experimental conditions which are variations about a base case of $V_{in} = 1{\cdot}56$ m/s,

Table 1
Summary of points A and B measurement conditions

Set no.	Mean nozzle velocity V_{in} (m/s)	Mould width W (mm)	Mould thickness H (mm)	Nozzle inner diameter d_i (mm)	Nozzle outer diameter d_o (mm)	SEN submergence S (mm)
1	1·56	80, 110, 130, 160, 230, 300, 390, 500	55	33	38	120
2	1·56	90, 160, 235, 300, 400, 500	80	33	38	120
3	1·56	100, 160, 230, 300, 400, 500	105	33	38	120
4	1·32	500	55, 80, 105	18	20	120
5	1·32	500	55, 80, 105	24	27	120
6	1·32	500	55, 80, 105	31	34	120
7	1·32	500	55, 80, 105	38	42	120

TABLE 2
Summary of PIV measurement conditions

Casting rate R (m/min)	Mould thickness H (mm)	SEN submergence S (mm)
2.0	80	20, 60, 120
1·0	80	20, 60, 120
2.0	38	120
2.0	55	120
2.0	105	120

$W = 500$ mm, $H = 80$ mm, $S = 120$ mm, with the glass SEN ($d_i = 33$ mm, $d_o = 38$ mm). This corresponds to a casting rate $R = 2$ m/min for the base case. In all cases, the SEN was positioned about the centre-line $x = 0$, $z = 0$.

Details of the LDA data and error analysis are given in Lawson & Davidson (1999), the PIV data analysis is described in Lawson & Davidson (1998*a*), and the PIV error analysis is given here in Appendix A.

3. NUMERICAL MODELLING

3.1. Model Formulation

Gebert *et al.* (1998*a*, *b*) developed a transient two-dimensional computational flow model of submerged injection into a thin rectangular cavity with outflow at the bottom of the cavity. Figure 3(a) shows a schematic of the computational model flow geometry. The Gebert model successfully predicted sustained oscillations of the jet when the in-flow was steady.

An essential feature of the numerical model, which permits the prediction of jet oscillation, is that it includes a representation of the cross-flow between the nozzle shaft and the broad face of the cavity wall. This is achieved in the two-dimensional model by representing the inlet flow as an internal mass source while allowing flow to occur past the region occupied by the nozzle. In Figure 3(a), the inlet is defined as the lower face of the small (black) rectangular region near the nozzle tip which is removed from the computational domain. The top and side faces of this tip region are taken to be no-slip boundaries. A velocity profile consistent with the $\frac{1}{7}$th power law for fully developed turbulent pipe flow is chosen at the inlet.

The remainder of the region occupied by the nozzle [the grey region in Figure 3(a)] is retained in the computational domain and is available for cross-flow. To account for the resistance to cross-flow resulting from the obstruction caused by the SEN, a resisting force of the form $K|\mathbf{u}|\mathbf{u}$, where K is a constant, is included in the momentum equation. The resistance coefficient K is taken to be zero everywhere except in the SEN region [grey area in Figure 3(a)]. The model geometry takes no account of the nozzle wall thickness, although this could be implemented if required.

The free surface is approximated by the top boundary of the computational domain which is taken to be a stationary, horizontal, free-slip boundary. No-slip boundary conditions together with wall functions are applied at solid walls. Turbulence is represented by the standard k–ε model. At the bottom boundary, which is the flow outlet, zero normal gradient conditions are applied.

3.2. Calculation Approach

To initiate a calculation a lateral perturbation is applied to the inlet velocity. This is not strictly necessary as systemic numerical perturbations were found to be sufficient to initiate

an oscillation; it just takes longer to occur than if the inlet velocity is perturbed. In each case calculations are continued until a regular cyclic flow behaviour is obtained.

The commercial fluid flow computer program CFX4 is used to calculate the model flow using finite volume methods on a nonuniform grid with increased mesh density near the nozzle. The solution is based on the SIMPLEC algorithm for the pressure correction. Advection of the turbulence variables k and ε is calculated using a van Leer flux limiter to prevent nonphysical negative values during the solution procedure and a consequent lack of numerical convergence. For all other transported variables, advection is based on the third-order QUICK scheme. Numerical details relating to the mesh density and tests for numerical accuracy are given in Gebert *et al.* (1998*a*).

4. RESULTS AND DISCUSSION

4.1. Cross-Flow Oscillation

4.1.1. Dependence on mould width

Figure 5 shows the measured and predicted frequency and peak velocity of cross-flow as a function of mould width W for varying mould thickness H. The frequency results are plotted in terms of a Strouhal number (St_d) based on nozzle internal diameter (d_i) and mean inlet velocity (V_{in}). The peak velocity results are scaled by V_{in}. The width W is scaled by the length ($L^* = 1050$ mm) of the model flow domain which is the distance from the free surface to the slot valve. A value of dimensionless resistance coefficient $Kd_i/\rho = 0{\cdot}594$ (based on $\rho = 1000\ \mathrm{kg/m^3}$) was used in the numerical model to give the "best" prediction for frequency in the base case ($W = 500$ mm and $H = 80$ mm).

The measurements show that the frequency of the cross-flow oscillation is independent of the three mould thicknesses considered ($H = 55, 80, 105$ mm), the only significant difference being that $H = 55$ mm resulted in an oscillation at the smallest mould width ($W/L^* = 0{\cdot}1$), whereas $H = 80$ and 105 mm did not. The frequency increases as the width of the mould is reduced, until a critical width is reached at which the oscillation stops. The predicted dimensionless frequency (St_d) compares well with the measured values. Like the experimental results for $H = 80, 105$ mm, no oscillation was predicted when $W/L^* = 0{\cdot}1$. It likely that the agreement between the predicted and experimental values can be improved in the lower range of W by adjusting the value chosen for Kd_i/ρ; however, this seems of little value since measurement errors for St_d are estimated to be in the range 7·6–13·8% assuming from previous work a measurement error in V_{in} of 3·3% and in f of 6·8–13·7% (Lawson & Davidson 1999).

Although the mould thickness H does not enter the flow calculation of the two-dimensional model, the value of H must be used to estimate a cross-flow velocity which can be compared with the value U_C measured in the gap ($H - d_o$) between the nozzle and the mould wall. The theoretical cross-flow velocity is taken to be

$$U_{cp} = \frac{U_{\mathrm{calc}}}{V_{\mathrm{Cin}}} \frac{Q}{Hd_i} \frac{H}{H - d_o}, \tag{1}$$

where U_{calc} is the horizontal velocity calculated at point A in the two-dimensional model, V_{Cin} is the value of the inlet velocity used in the 2-D numerical model, and Q denotes the volumetric flow rate through the nozzle into the mould. Multiplying $U_{\mathrm{calc}}/V_{\mathrm{Cin}}$ by Q/Hd_i gives the velocity which would be obtained by assuming that the two-dimensional model is a planar section of a mould geometry of thickness H. The multiple $H/(H - d_o)$ accounts for the gap width ($H - d_o$) actually available for cross-flow compared with the mould

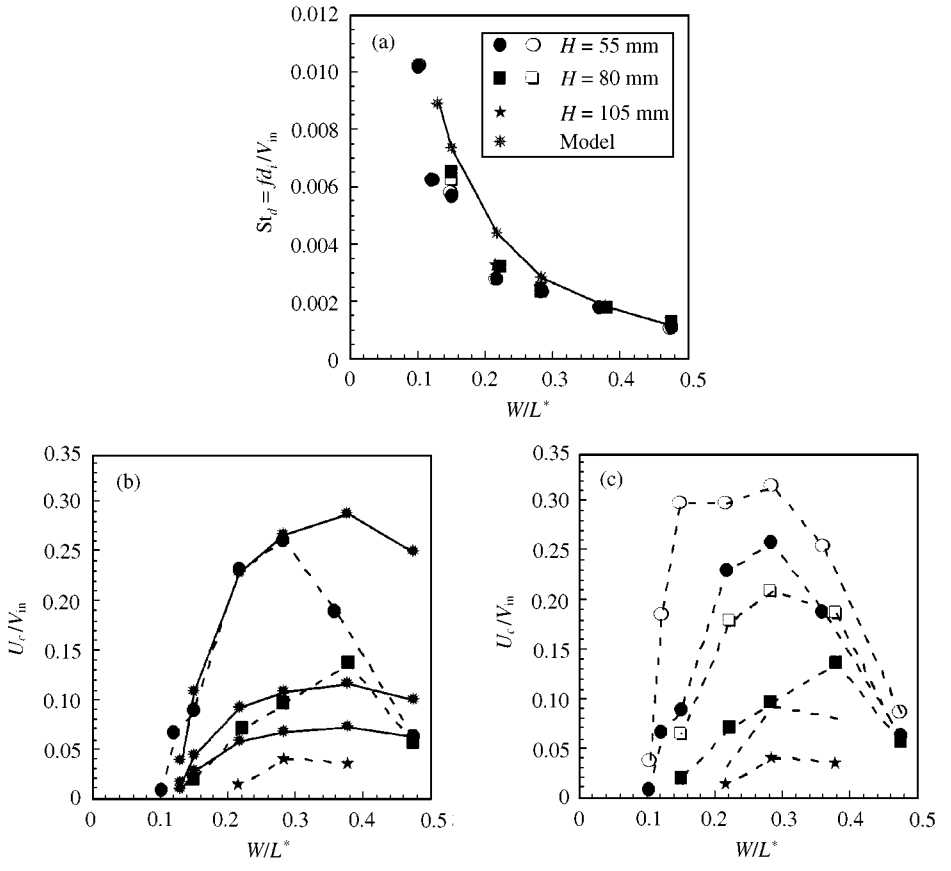

Figure 5. (a) Variation of cross-flow oscillation dimensionless frequency (expressed as a Strouhal number based on nozzle diameter) with width W for different mould thicknesses H; (b) comparisons of experimental and computational dimensionless peak cross-flow velocity U_c with width W for different mould thicknesses H; (c) variations of dimensionless peak cross-flow velocity U_c with width W for different mould thicknesses H; $V_{in} = 1{\cdot}56$ m/s, $S = 120$ mm, $d_i = 33$ mm, $d_o = 38$ mm. Corresponding black and white symbols denote measurements at points A and B, respectively. Velocities are scaled by the average velocity V_{in} at the SEN exit. The solid line shows predictions derived from the two-dimensional model.

thickness H and it is this which accounts for the increase in cross-flow velocity as H decreases. Logical choices for V_{Cin} include V_{in} and Q/Hd_i; however, the value of V_{Cin} is not important because the dimensionless velocity field calculated (U_{calc}/V_{Cin}) is independent of that choice.

Figure 5(b) compares the predicted (U_{cp}) and experimental (U_c) peak cross-flow velocities at point A, normalized by the experimental inlet velocity, as a function of W for the $H = 55$, 80, 105 mm. The comparisons are reasonable considering the inability of a two-dimensional model to predict the detailed out-of-plane flow past the nozzle. The predicted curve for $H = 55$ mm exhibits a maximum as does the experimental data; however, the calculated maximum is less pronounced and is displaced. When $W = 500$ mm, the cross-flow is significantly over-predicted, with the difference being much greater for $H = 55$ mm than it is for $H = 80$ mm. Presumably, this occurs because the cross-flow velocity profile is less flat [and equation (1) less applicable] when the gap ($H - d_o$) between the SEN and the broad

face of the mould is reduced (Lawson & Davidson 1999). The specific reason why the cross-flow velocity prediction becomes substantially different from the measured values when $W = 500$ mm is not known. Attempts to account for the difference by incorporating an approximation to the wall friction on the broad faces of the mould into the 2-D numerical model did not improve the prediction.

Figure 5(c) compares measured peak cross-flow velocities at points A and B. Values at point B are for cross-flow below the nozzle in the gap between the jet and the cavity wall. Predictions of point B cross-flow are not possible with the present two-dimensional model because it does not allow for (out-of-plane) cross-flow which bypasses the jet in the region between the jet and the cavity wall. To do so in a two-dimensional model would require a secondary flow path across the jet which did not simultaneously interfere with the main jet flow. A secondary path for cross-flow at point A is only possible because it traverses the nozzle region in which no primary flow is being calculated. Note that the peak velocity values at any given data-point are taken from a mean oscillation cycle obtained by averaging the LDA velocity data using the known cross-flow period. Figure 5(c) shows that cross-flow is greater at point B than at point A, presumably because the gap at point B has a fluid boundary on one side, and hence offers a lower resistance to flow than at point A.

The cross-flow velocity data at both points A and B in Figure 5 exhibit maxima, with the lowest values occurring at the largest and smallest values of W/L^* in each case. No data are shown for $W/L^* < 0{\cdot}2$ and $W/L^* > 0{\cdot}4$ when $H = 105$ mm, as no oscillation occurred in those cases. The maxima in the cross-flow velocities for varying mould width W occur because the oscillation should cease when W has limiting small or large values. The smallest mould width theoretically possible is $W = d_o$. In that case, no cross-flow is physically possible, and no oscillation will occur. At the other extreme, if the side walls are removed ($W \to \infty$), the flow is similar to a free two-dimensional jet, and the recirculation cells on either side of the jet will not form. In that case, cross-flow should again be zero, since cross-flow results from pressure differences linked to the changing angular momentum of the recirculation cells during the oscillation (Lawson & Davidson 1999).

4.1.2. Dependence on nozzle diameter

Figure 6 shows the measured and predicted response of the cross-flow oscillation to changes in nozzle internal diameter d_i for a fixed nozzle fluid velocity and mould width. The corresponding outer diameters are 2–4 mm greater than d_i, as shown in Table 1. In this figure, frequency results are plotted in terms of a Strouhal number (St_w) based on the mould width W and the mean inlet velocity V_{in}. The variation in the predicted Strouhal number (St_w), based on a dimensionless resistance coefficient $Kd_i/\rho = 0{\cdot}594$ as before, compares very well with the experimental values.

The measured frequency shown in Figure 6(a) is independent of mould thickness H, at least for $H = 55$ and 80 mm. The frequency increases with nozzle diameter because the volumetric flow rate (and hence the casting rate) increases, and the frequency in known to increase with increasing casting rate (Lawson & Davidson 1998*a*, *b*). Results for $H = 105$ mm are not shown because spectral analysis of the LDA data did not indicate any dominant frequency in the cross-flow region for this value of W (500 mm).

The measured cross-flow velocities shown in Figure 6(b) also increase with nozzle diameter, because the volumetric flow rate increases. The cross-flow velocity past the jet at point B is greater than that past the nozzle at point A for the same reason that it is greater in Figure 5(c) resistance to cross-flow at point B is lower than at point A, as explained before. The difference between the cross-flow velocities at points A and B is greater when $H = 55$ mm than it is when $H = 80$ mm, and it increases as the nozzle diameter increases.

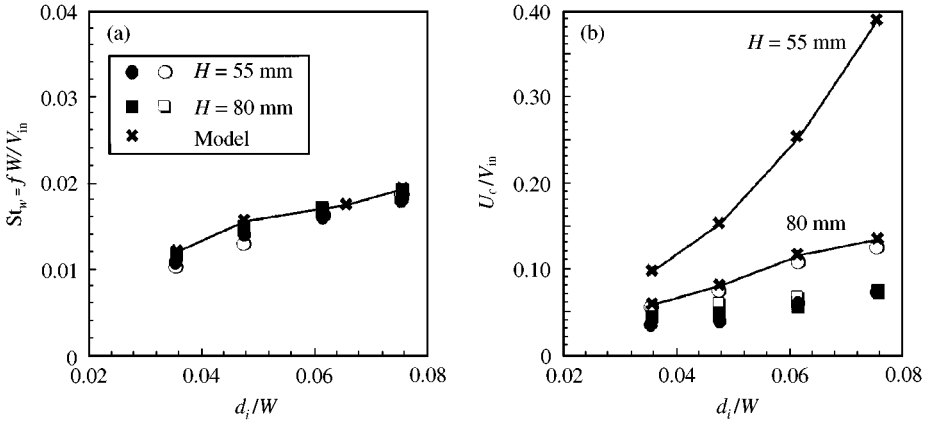

Figure 6. (a) Variation of cross-flow oscillation frequency (expressed as a Strouhal number based on mould width) and (b) variation of dimensionless peak cross-flow velocity with nozzle inner diameter d_i for two different mould thicknesses H; $V_{in} = 1{\cdot}32$ m/s, $W = 500$ mm, $S = 120$ mm. The black and while symbols denote measurements at points A and B, respectively. Velocities are scaled by the average velocity V_{in} at the SEN exit. The solid line shows the values predicted by the two-dimensional model with $Kd_i/\rho = 0{\cdot}594$.

This occurs because reducing H and increasing nozzle diameter each reduce the gap available for cross-flow. A consequence is that cross-flow increasingly favours the path of lower resistance at point B.

The predicted cross-flow velocities at point A are determined from the numerical calculation according to equation (1) which models the effect of mould thickness H. Predictions for both $H = 55$ and 80 mm correctly predict an increase in cross-flow with increasing SEN diameter, but they over-estimate the magnitude of cross-flow in each case. This over-estimate is greater for $H = 55$ mm than it is for $H = 80$ mm, consistent with the prediction in Figure 5(c) for $W = 500$ mm. The degree of over-prediction increases as the SEN diameter increases and the cross-flow velocity profile in the (decreasing) gap between the nozzle and broad face of the mould becomes more pronounced (Lawson & Davidson 1999); in that case equation (1) becomes less applicable earlier.

4.1.3. Dependence on geometric scaling

If all dimensions of the flow domain are scaled identically (geometric similarity) then we would expect the Strouhal number (dimensionless frequency) to be unchanged. If the fluid velocity entering the mould is also varied, we expect the Strouhal number to be independent of Reynolds number (Re), since Re is large so that viscous effects are confined to thin boundary layers at the walls. Figure 7 shows the effect on Strouhal number of varying the fluid velocity for different geometric scaling factors. All dimensions are scaled identically except the effective cavity length L^* which was fixed at 1050 mm. Unfortunately, the experimental rig was not constructed to vary the length conveniently. From Figure 7(a), the Strouhal number is shown to be independent of Reynolds number for each scaling factor. Such Reynolds number independence has also been demonstrated for the numerical model. However, the measured Strouhal number increases as the scaling factor increases. This occurs because geometric similarity is not maintained (L^* is fixed).

A measure of the dependence of the Strouhal on the scaling in Figure 7(a) is given in Figure 7(b) where Strouhal number is shown to decrease with increasing L^*/W. This is

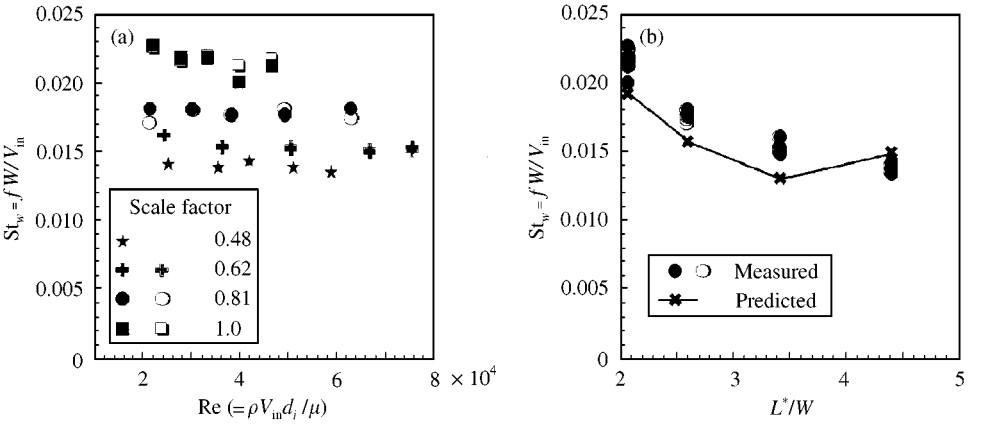

Figure 7. (a) Variation of cross-flow oscillation frequency (expressed as a Strouhal number based on mould width) with Reynolds number and (b) variation of Strouhal number with cavity length/width ratio. All dimensions of the model apart from length L^* are scaled by a factor. When the scaling factor is 1·0, $W = 500$ mm, $H = 80$ mm, $S = 120$ mm, and $d_i = 38$ mm. Corresponding black and white symbols denote measurements at points A and B, respectively. The solid line shows the values predicted by the two-dimensional model with $Kd_i/\rho = 0{\cdot}594$.

consistent with the scaling factor dependence in Figure 7(a). If geometric similarity was maintained, there should be no dependence on L^*/W. The dependence on scaling factor predicted by the numerical model, based on dimensionless resistance coefficient $Kd_i/\rho = 0{\cdot}594$, shows acceptable agreement with the measured Strouhal number in Figure 7(b). The predicted increase in Strouhal number when $L^*/W = 4{\cdot}5$ occurs when the scaling factor is smallest and the gap width in the actual experiment is only 9 mm. In that case, viscous effects could influence the value of the resistance coefficient K so that a value larger than that derived by scaling (i.e. by fixing Kd_i/ρ) becomes appropriate. A sufficiently larger K value will reduce the predicted frequency so that it continues to decrease when $L^*/W = 4{\cdot}5$.

4.1.4. Stability map

The stability map in Figure 8 shows the observed regions of stable, unstable, and no oscillation for varying relative dimensions of the cavity. (However, note that the effective cavity length L^* is fixed at 1050 mm). An unstable oscillation is defined as one in which the signal-to-noise ratio from the spectral peak analysis lies in the range 0–20 dB. Signal-to-noise levels above 20 dB are defined as a jet oscillation and ensure sufficient accuracy levels are met from the signal peak analysis (Lawson & Davidson 1999; Bobroff 1986). We see that the oscillation eventually ceases as the nozzle diameter d_i or the cavity thickness H becomes an increasing fraction of the cavity width W. In particular, no oscillation is observed when $H/W > 0{\cdot}6$ or $d_i/W > 0{\cdot}4$. The oscillation also ceases for $H/W < 0{\cdot}04$. Note that the absence of oscillation reported above for the smallest and largest W values in Figure 5 is represented in the stability map of Figure 8.

4.1.5. Comparison with frequency of related flows

Self-sustained oscillations occur in a wide range of flows involving impinging or obstructed shear layers. These include the interaction of jets with edges, orifices and surfaces, resonant

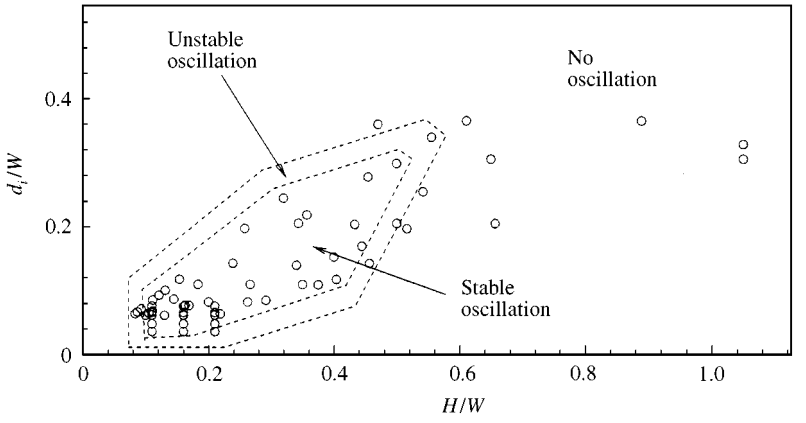

Figure 8. Stability map for varying nozzle diameter/cavity width (d_i/W) and cavity thickness/width ratios (H/W) for fixed effective cavity length $L^* = 1050$ mm.

oscillations in cavities, and confined jet flow. Rockwell & Naudascher (1979) and Rockwell (1983) have reviewed the main results for wide variety of configurations.

A confined jet is an example of a shear layer bounded by a recirculation zone which can exhibit oscillations driven by the hydrodynamic instability of the shear layer ($St \sim O(1)$ based on impingement length), or oscillations of much lower frequency ($St \ll 1$) generated by other mechanisms (Rockwell 1983). The flapping oscillations reported here are of the low-frequency variety with Strouhal numbers $St_d \sim 0{\cdot}002$–$0{\cdot}01$ based on nozzle diameter. These are about two orders of magnitude smaller than the Strouhal numbers of shear-generated structures formed in a jet for which $St_d \sim 0{\cdot}3$–$0{\cdot}8$ (Nathan *et al.* 1998). This order of magnitude difference has been found for low-frequency oscillations in other flows, viz. confined jet precession (Nathan *et al.* 1998), and flapping motion of a jet entering a suddenly enlarged rectangular (Villermaux & Hopfinger 1994) or planar passage (Shakouchi 1989), or blind cavity (Shakouchi *et al.* 1982). Nathan *et al.* (1998) discuss this difference in some detail and conclude that the low-frequency oscillation is a quite different phenomenon from that of shear-generated instability, being associated with the motion of the jet as a whole rather than structures within the jet.

The trends predicted by Shakouchi (1989) for the flapping motion of a rectangular jet entering a planar sudden expansion can be compared qualitatively with those obtained here. An increasing frequency with decreasing cavity width, shown here in Figure 5(a), is also found by Shakouchi (1989). The oscillation frequency increases here with increasing nozzle diameter [Figure 6(a)]. Again a similar trend was found by Shakouchi (1989) as the width of the two-dimensional nozzle was increased. However, his frequency results also show a dependence on cavity thickness H, unlike the present work, although both studies find that the choice of H (and other dimensions) determines whether an oscillation will occur or not (Figure 8).

4.2. Jet Flow

Figure 9(a) shows measured and predicted radial profiles of the mean downwards velocity in the jet just below the nozzle tip ($y = -32$ mm) for different nozzle diameters and a fixed flow rate. Measured dimensionless velocity profiles are found to be insensitive to the nozzle diameter. This is expected close to the nozzle tip since the dimensionless inlet velocity

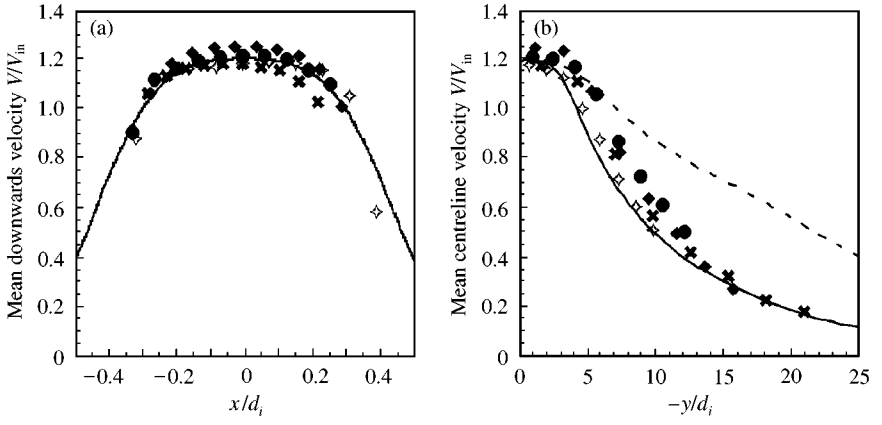

Figure 9. (a) Horizontal profile of mean downwards jet velocity at $y = -32$ mm, $z = 0$ below the nozzle exit, and (b) mean downwards centreline velocity of the jet, for varying nozzle inner diameter d_i and fixed volumetric flow rate (casting rate $R = 1$ m/min, $W = 500$ mm, $H = 80$ mm, $S = 120$ mm). Velocities are scaled by the corresponding average velocity V_{in} at the SEN exit. The solid lines show the values predicted by the two-dimensional model for $d_i = 33$ mm with $Kd_i/\rho = 0{\cdot}594$. The dashed line corresponds to predictions from a flow model which is constrained to be steady and symmetric. ×, $d_i = 18$ mm; ◆, $d_i = 24$ mm; ●, $d_i = 31$ mm; ◇, $d_i = 38$ mm.

should be the same in all cases because the flow pattern away from solid walls is Reynolds number independent at high Reynolds number. The close agreement achieved by the corresponding model prediction for a 33 mm nozzle verifies the validity of the $\frac{1}{7}$th power-law velocity profile (corresponding to fully developed turbulent pipe flow) chosen at the model inlet.

Corresponding measured and predicted mean centre line velocities are shown in Figure 9(b). Again the dimensionless velocity variation is not sensitive to the choice of nozzle diameter. The solid line represents the model prediction when the nozzle diameter is 33 mm. Agreement with the experimental values is satisfactory with the model under-predicting the centreline velocity slightly at intermediate values of y/d_i. If the model flow field is constrained to be steady and symmetric about the vertical axis, the predicted velocity on the centre-line (dashed line) is too large, and corresponds to the reduced lateral momentum transfer which will occur in the absence of an oscillation.

Figure 10 shows measured and predicted turbulence characteristics for the cases displayed in Figure 9 (varying nozzle diameter, fixed flow rate). The radial profile of turbulence intensity [Figure 10(a)] based on the local r.m.s. and mean velocities just below the nozzle tip are shown to be insensitive to the nozzle diameter, just as the mean velocity profiles are. The r.m.s velocity predicted by the numerical model is calculated as $(2k/3)^{1/2}$ and ignores any contribution from the primary oscillation which is very small close to the nozzle. The predicted turbulence intensity profile lies slightly below the measured one, indicating that the actual turbulence intensity at the nozzle tip is somewhat greater than that for fully developed pipe flow.

Corresponding measured and predicted r.m.s. velocities on the centre line are shown in Figure 10(b, c), scaled according to the mean nozzle velocity. No predictions are shown in Figure 10(c), because the two-dimensional model cannot predict out-of-plane velocities. As before, the dimensionless velocity profiles are not sensitive to nozzle diameter. The solid line in Figure 10(b) shows the model prediction when the nozzle diameter is 33 mm. The agreement with experiment is reasonable considering that turbulence characteristics are

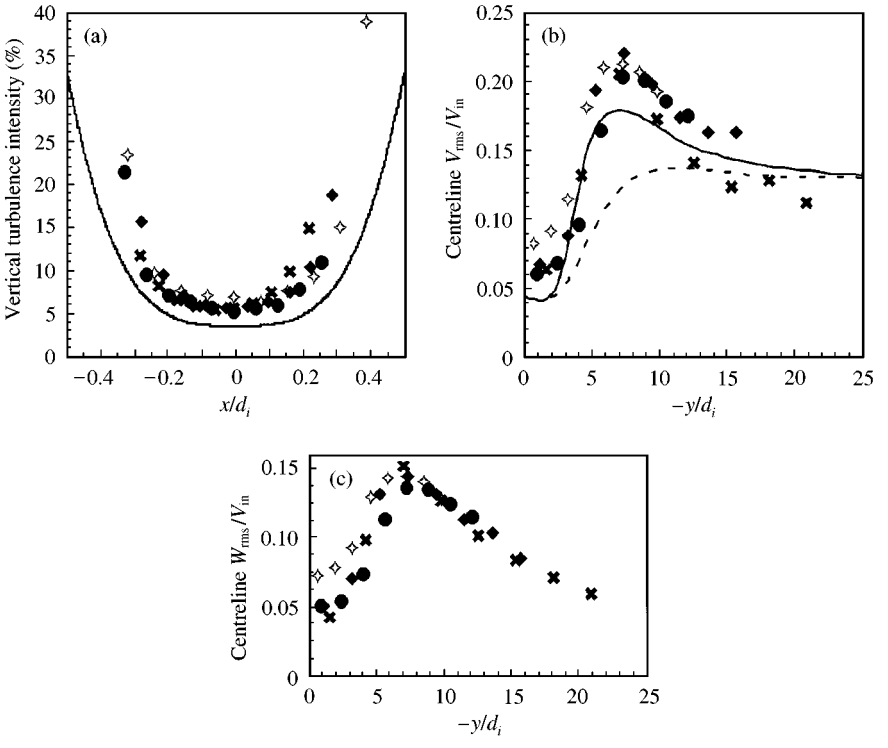

Figure 10. (a) Horizontal profile of vertical turbulence intensity in the jet at $y = -32$ mm, $z = 0$ below the nozzle exit; (b) r.m.s. of vertical velocity of the jet along the centre-line; (c) r.m.s. of transverse velocity of the jet along the centre-line and perpendicular to the broad face of the mould, for varying nozzle inner diameter d_i and fixed volumetric flow rate (casting rate $R = 1$ m/min, $W = 500$ mm, $H = 80$ mm, $S = 120$ mm). Velocities are scaled by the corresponding average velocity V_{in} at the SEN exit. The solid lines show the values predicted by the two-dimensional model for $d_i = 33$ mm with $Kd_i/\rho = 0{\cdot}594$. The dashed line corresponds to predictions from a flow model which is constrained to be steady and symmetric.

typically less well represented than the mean flow. Ignoring the contribution of the oscillation to the calculated r.m.s. value will become less valid away from the nozzle tip.

The centreline r.m.s. velocity variation shown in Figure 10(b, c) rises to a peak with vertical distance from the nozzle tip before falling again. Although the transient numerical model also predicts this behaviour, the steady symmetric numerical model [dashed line, Figure 10(b)] does not. The steady model only predicts an increase in the r.m.s. velocity to a constant value downstream. Both transient and steady models approach the same downstream value. The different behaviour of the steady model indicates that the peak occurring in the centreline r.m.s. velocity at about seven nozzle diameters below the nozzle tip results from enhancement of turbulence by the oscillation of the jet. Note that the peak lies at the same distance from the nozzle tip as the transition point between the potential core and complete turbulence in a free jet.

Figure 11 shows dimensionless measured and predicted horizontal profiles of the downwards velocity at selected distances below the nozzle tip. The transient numerical model prediction agrees well with the corresponding measured values. There is a slight over-prediction away from the centre with increasing distance, and an under-prediction at the centreline consistent with Figure 9(b). Also consistent with Figure 9(b), is the

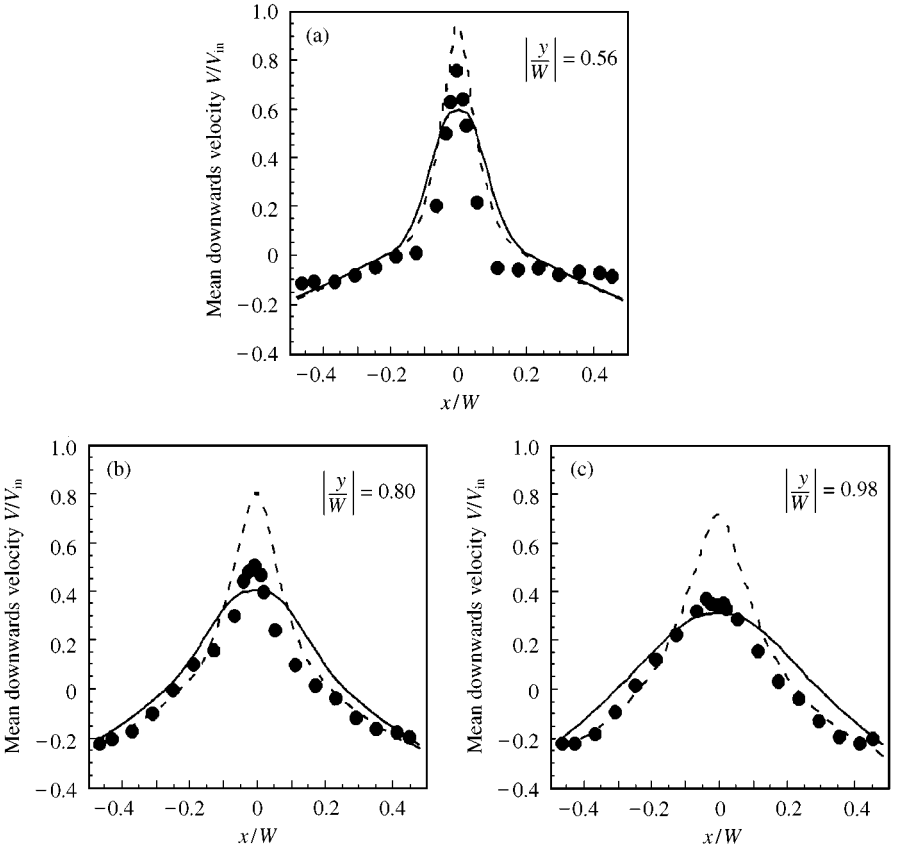

Figure 11. Horizontal profiles of the mean downwards jet velocity at (a) $y = 280$, (b) 400 and (c) 490 mm, for the base configuration (parameters: $V_{in} = 1{\cdot}56$ m/s, $S = 120$ mm, $H = 80$ mm, $W = 500$ mm, $d_i = 33$ mm). Velocities are scaled by the average velocity V_{in} at the SEN exit. The solid lines show the values predicted by the two-dimensional model with $Kd_i/\rho = 0{\cdot}594$. The dashed line corresponds to predictions from a flow model which is constrained to be steady and symmetric.

over-prediction of the peak at the centre by the steady numerical model since it does not account for momentum dispersion by the oscillation. This over-prediction is least nearer the nozzle tip because the oscillation is smaller there (right at the nozzle tip there is no oscillation as the in-flow is steady). Note that the steady model actually gives a better prediction of the mean velocity away from the centreline than the transient model does. However, the transient model gives a better overall prediction.

Figure 12 shows vector plots derived from PIV measurements in the cross-flow region (top panels) and in the jet region (bottom panels). These measurement regions are identified in Figure 3(b). The plots show the flow field at 1/4 cycle intervals and illustrate the oscillation behaviour. This behaviour has been described by Lawson & Davidson (1999). Briefly, two recirculation cells, one on each side of the jet, move up and down in phase with the jet deflection and the cross-flow. For example, in the part of the cycle depicted by Figure 12(a, b), the jet is moving to the left, cross-flow is from left to right, the left circulation cell is rising and the right one is falling. The angular momentum of the left cell increases as it rises due to the action of the jet shear layer, causing the pressure in the left cell to decrease. Conversely, the angular momentum of the right cell decreases as it falls because of the

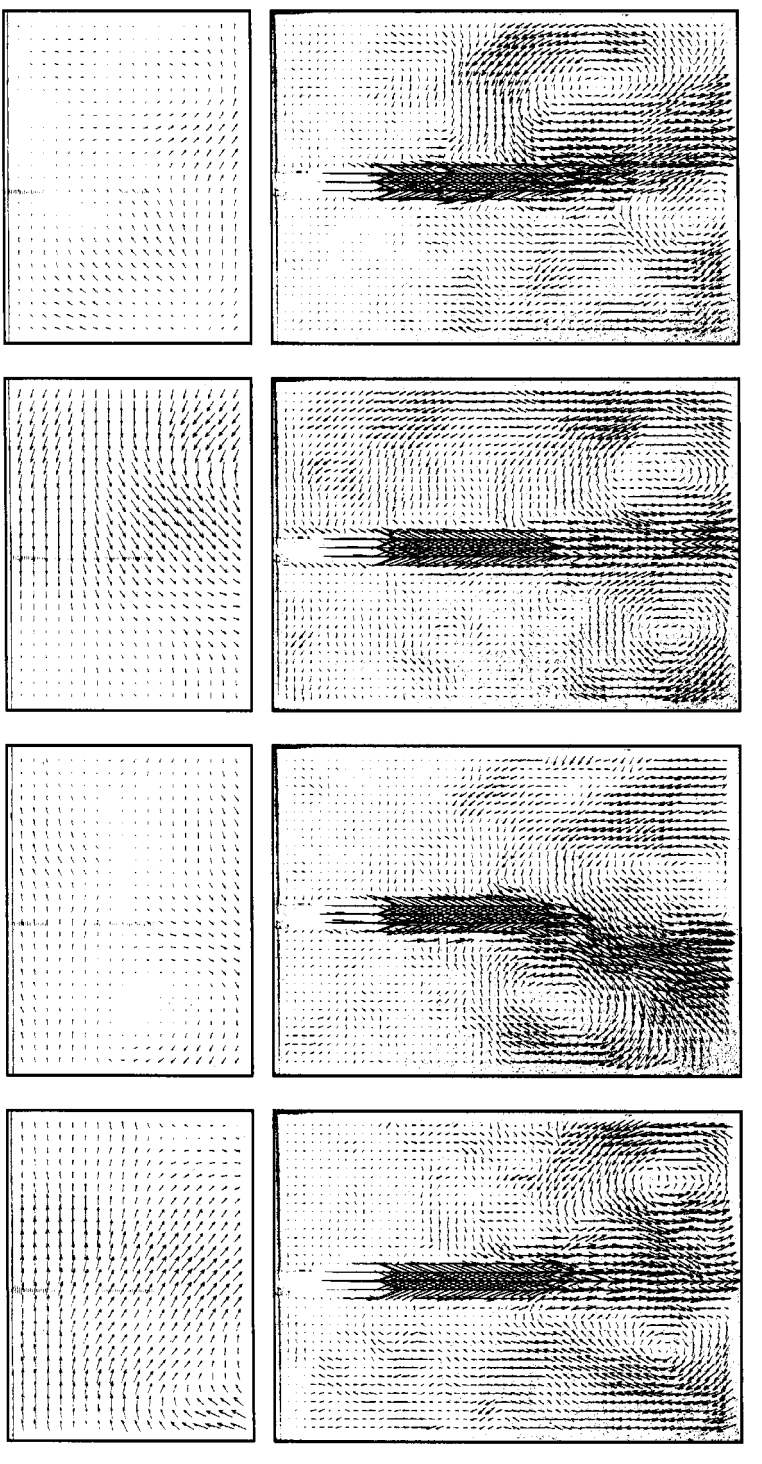

Figure 12. PIV vector flow field in the jet and cross-flow regions at 1/4 cycle intervals for $W = 500$ mm, $H = 80$ mm, $S = 120$ mm, $d_i = 33$ mm, $V_{in} = 1{\cdot}56$ m/s. In that case, the measured period of the cross-flow oscillation is 18 s.

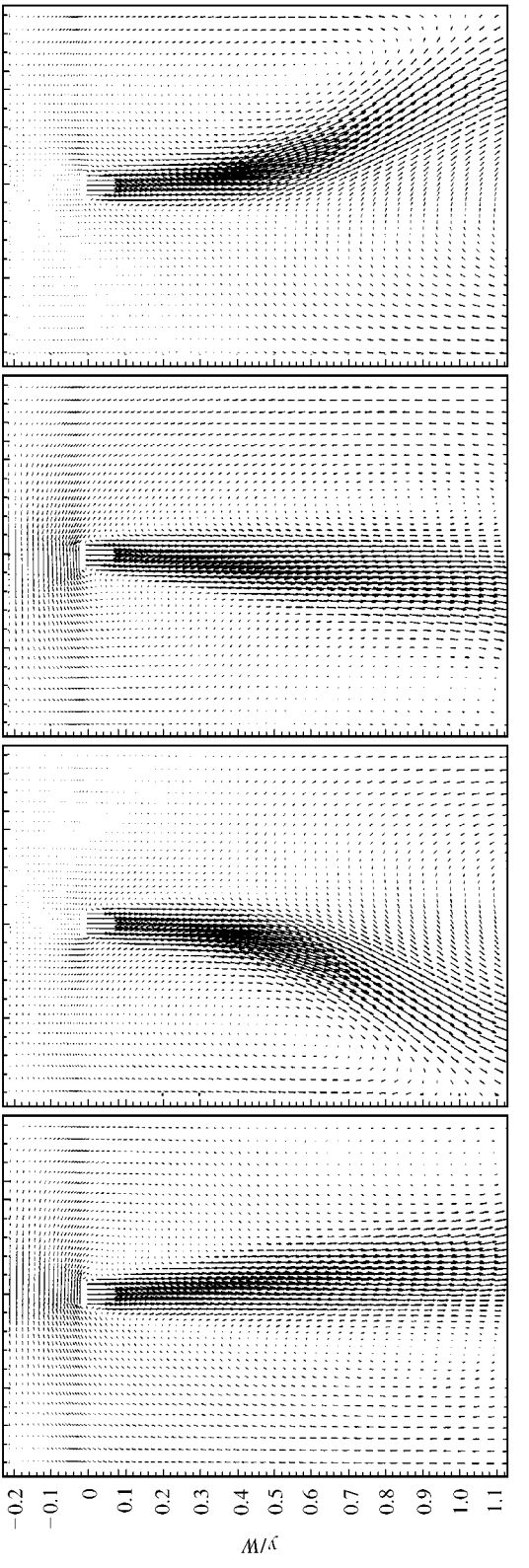

Figure 13. Vector plots of the predicted flow field at 1/4 cycle intervals for the geometry specified in Figure 12. Axes, relative to an origin at the nozzle tip, are scaled by the cavity width W. The magnitude of reference vector is V_{in}, the mean velocity at the nozzle exit.

decaying jet profile, causing the pressure in the right cell to increase. The resulting pressure difference reinforces the leftwards deflection of the jet, while simultaneously retarding the left-to-right cross-flow. Eventually, the cross-flow reduces to zero at a configuration close to that shown in Figure 12(b), after which the side-to-side motion of both the cross-flow and the jet reverses direction. The (now right-to-left) cross-flow increases as the jet swings back towards the vertical [Figure 12(c)]. The subsequent behaviour in the part of the cycle depicted by Figure 12(c, d) is the mirror image of that described above. Further discussion on the mechanism of the oscillation is given by Lawson & Davidson (1999).

Figure 13 shows vector plots of the predicted flow field at 1/4 cycle intervals synchronized as closely as possible to the cycle shown in Figure 12. Qualitative features common in both the predicted and measured flow fields include the displacement of the jet, the increased cross-flow when the jet is near vertical and the reduced cross-flow when the jet is near maximum displacement. Inspection of the predicted flow field also shows recirculation cells on each side of the jet as is expected. Quantitative comparisons between the predicted and measured flow fields have already been made in Figures 9–11.

5. CONCLUSION

This work has presented a combined experimental and computation study of a low Strouhal number ($St < 0{\cdot}02$), self-sustained oscillating jet emanating from a nozzle submerged in a thin rectangular cavity. The use of the advanced experimental techniques LDA and PIV has allowed detailed pointwise and full-field velocity data to be recorded for a range of mould widths, mould thicknesses and nozzle diameters. This temporal and spatial velocity data has been directly compared with predictions from a two-dimensional transient numerical flow model of the system.

The model gives good predictions of the frequency characteristics of the cross-flow associated with the jet oscillation for mould width-to-length ratios in the range 0·1–0·5 and for nozzle diameter to mould width ratios in the range 0·38–0·75. However, peak cross-flow velocity characteristics were found harder to predict, with the greatest discrepancies occurring at values of mould width-to-length ratios above 0·3 and mould depths greater than 80 mm. These discrepancies were attributed to three-dimensional effects in the cross-flow region which could not be simulated by the 2-D model.

Examination of the flow field in general, including the jet and the recirculation cells, showed close agreement between the numerical model and experimental turbulence and mean velocity data. The experimental results also showed jet oscillation to be stable for a range of nozzle-diameter/cavity-width ratios of 0·05–0·3 and cavity thickness/width ratios 0·1–0·5. Outside this range the jet either did not oscillate in a stable manner or did not oscillate at all. Work is ongoing to enhance the ability of the numerical model to capture these flow features.

ACKNOWLEDGEMENT

This work was supported by the Australian Research Council using facilities provided by the G.K. Williams Cooperative Research Centre for Extractive Metallurgy, a joint venture between the CSIRO Division of Minerals and the Department of Chemical Engineering at the University of Melbourne. The authors would also like to thank Mr Tim Berrigan and the workshops of the Department of Chemical Engineering for their help and support during the project.

References

ADRIAN, R. J. 1986 Image shifting technique to resolve directional ambiguity in double-pulsed velocimetry. *Applied Optics* **25,** 3855–3858.

ADRIAN, R. J. 1991 Particle-imaging techniques for experimental fluid mechanics. *Annual Review of Fluid Mechanics* **23,** 261–304.

AUSTIN, P. R. 1992 Literature survey on modelling of continuous casting. BHP Research Unrestricted Report BHPR/PMR/R/92/044.

BOBROFF, N. 1986 Position measurement with a resolution and noise limited instrument. *Review of Scientific Instruments* **57,** 1152–1157.

DRING, R. P. 1982 Sizing criteria for laser anemometry particles. *ASME Journal of Fluids Engineering* **104,** 15–17.

DURST, F., MELLING, A. & WHITELAW, J. H. 1981 *Principles and Practice of Laser Doppler Anemometry*, Second Edition. London: Academic Press.

ESPEDAL, A. B. & RODER, R. 1993 Prospects of thin gauge high-speed strip casting technology. In *Proceedings Third Australian–Asian–Pacific Course and Conference on Aluminium Cast House Technology, Theory & Practice* (ed. M. Nilmani), pp. 303–319. Melbourne, Australia: TMS.

GEBERT, B. M., DAVIDSON, M. R. & RUDMAN, M. J. 1998*a* Computed oscillations of a confined submerged liquid jet. *Applied Mathematical Modelling* **22,** 843–850.

GEBERT, B. M., DAVIDSON, M. R. & RUDMAN, M. J. 1998*b* Calculation of an oscillating liquid jet in a two-dimensional cavity. *Computational Techniques and Applications: CTAC-97*, (eds J. Noye, M. Teubner & A. Gill), pp. 217–224. Singapore: World Scientific.

GUPTA, D. & LAHIRI, A. K. 1994 Water Modelling study of the surface disturbances in continuous slab caster. *Metallurgical and Materials Transactions* **25B,** 227–233.

HERBERTSON, J., HE, Q. L., FLINT, P. J. & MAHAPATRA, R. B. 1991 Modelling of metal delivery to continuous casting moulds. *1991 Steelmaking Conference Proceedings,* Washington, DC: Vol. 74, pp. 171–185. Iron and Steel Society.

HONEYANDS, T. A., LUCAS, J. & CHAMBERS, J. 1992 Preliminary modelling of steel delivery to thin slab caster moulds. *1992 Steelmaking Conference Proceedings*, Vol. 75, pp. 451–459. Toronto: Iron and Steel Society.

HONEYANDS, T. A. 1994 Flow dynamics in thin slab caster moulds. Ph.D. Dissertation, University of Newcastle, Australia.

HONEYANDS, T. A. & HERBERTSON, J. 1995 Flow dynamics in thin slab caster moulds. *Steel Research* **66,** 287–293.

HUANG, X., THOMAS, B. G. & NAJJAR, F. M. 1992 Modelling superheat removal during continuous casting of steel slabs. *Metallurgical Transactions* **23B,** 339–356.

KEANE, R. D. & ADRIAN, R. J. 1992 Theory of cross correlation analysis of PIV images. *Journal of Applied Scientific Research* **49,** 191–215.

LANDRETH, C. C. & ADRIAN, R. J. 1988 Measurement and refinement of velocity data using high image density analysis in particle image velocimetry. In *Proceedings of the Fourth International Symposium on the Applications of Laser Anemometry to Fluid Mechanics* (eds R. J. Adrian, T. Asanuma, D. F. G. Durao, F. Durst, J. Whitelaw), pp. 491–497, Lisbon, Portugal.

LAWSON, N. J., COUPLAND, J. M. & HALLIWELL, N. A. 1997 A generalised optimisation method for double pulsed particle image velocimetry. *Optics and Lasers in Engineering* **27,** 637–656.

LAWSON, N. J. & DAVISON, M. R. 1998*a* Measurement of cross-flow characteristics from a transient water model of a thin slab casting mould. *IMechE Optical Methods and Data Processing in Heat and Fluid Flow* (eds Bryanston-Cross *et al.*), pp. 301–310. London: IMechE.

LAWSON, N. J. & DAVISON, M. R. 1998*b* The application of LDA to characterise cross-flow from an oscillating jet in a thin slab casting mould. In *Proceedings 13th Australasian Fluid Mechanics Conference* (eds M. C. Thompson & K. Hourigan), pp. 667–670, Melbourne, Australia.

LAWSON, N. J. & DAVISON, M. R. 1999 Cross-flow characteristics of an oscillating jet in a thin slab casting mould. *ASME Journal of Fluids Engineering* **121,** 588–595.

LAWSON, N. J. & LIOW, J. -L. 1998 Low-cost design of 35mm drum camera for high-resolution, high-speed image analysis. *Review of Scientific Instruments* **69,** 4195–4197.

LECORDIER, B., MOUQALLID, M., VOTTIER, S., ROULAND, E., ALLANO, D. & TRINITE, M. 1994 CCD recording method for cross-correlation PIV development in unstationary high speed flow. *Experiments in Fluids* **1,** 205–208.

MAUREL, A., ERN, P., ZIELINSKA, B. J. A. & WESFREID, J. E. 1996 Experimental study of self-sustained oscillations in a confined jet. *Physical Review E* **54,** 3643–3651.

MOLLOY, N. A. 1969 Oscillatory flow of a jet into a blind cavity. *Nature* **224,** 1192–1194.

MORRIS, G. J., JUREWICZ, J. T. & PALMER, G. M. 1992 Gas–solid flow in a fluidically oscillating jet. *ASME Journal of Fluids Engineering* **114,** 362–366.
NAJJAR, F. M., THOMAS, B. G. & HERSHEY, D. E. 1995 Numerical study of steady turbulent flow through bifurcated nozzles in continuous casting. *Metallurgical and Materials Transactions* **26B,** 749–764.
NATHAN, G. J., HILL, S. J. & LUXTON, R. E. 1998 An axisymmetric 'fluidic' nozzle to generate jet precession. *Journal of Fluid Mechanics* **370,** 347–380.
NILLES, P. & ETIENNE, A. 1991 Continuous casting today — status and prospects. *Metallurgical Plant and Technology International* **6,** 56–67.
PICKERING, C. J. D. & HALLIWELL, N. A. 1985 Particle image velocimetry: a new field measurement technique. In *Optical Measurement in Fluid Dynamics*, Institute of Physics Conference Series no. 77, session 4. Bristol: Adam Hilge.
ROCKWELL, D. & NAUDASHER, E. 1979 Self-sustained oscillations of impinging free shear layers. *Annual Review of Fluid Mechanics* **11,** 67–94.
ROCKWELL, D. 1983 Oscillations of impinging shear layers. *AIAA Journal* **21,** 645–664.
SAMARASEKERA, I. V., THOMAS, B. G. & BRIMACOMBE, J. K. 1997 The frontiers of continuous casting. In *Proceedings of the Julian Szekely Memorial Symposium on Materials Processing*, Cambridge, MA (eds H. Y. Sohn, J. W. Evans & D. Apelian), pp. 275–297. The Minerals Metals and Materials Society.
SEYEDEIN, S. H. & HASAN, M. 1997 A three-dimensional simulation of coupled turbulent flow and macroscopic solidification heat transfer for continuous slab casters. *International Journal of Heat and Mass Transfer* **40,** 4405–4423.
SHAKOUCHI, T., SEUMATSU, Y. & ITO, T. 1982 A study on oscillatory jet in a cavity. *Bulletin of the JSME* **25,** 1258–1265.
SHAKOUCHI, T. 1989 A new fluidic oscillator, flowmeter, without control port and feedback loop. *ASME Journal of Dynamic Systems, Measurement and Control* **111,** 535–539.
THOMAS, B. G., MIKA, L. J. & NAJJAR, F. M. 1990 Simulation of fluid flow inside a continuous slab-casting machine. *Metallurgical Transactions* **21B,** 387–400.
VIETS, H. 1975 *Flip-flop jet design. AIAA Journal* **13,** 1375–1379.
VILLERMAUX, E. & HOPFINGER, E. J. 1994 Self-sustained oscillations of a confined jet: a case study for the non-linear delayed saturation model. *Physica D* **72,** 230–243.

APPENDIX A: PIV ERROR ANALYSIS

For a 2-D PIV system the velocity error originates from the recording and data processing stages. In the following simplified analysis, the recording stage error will be restricted to the error due to the seeding response to flow fluctuations, $\delta(e_V)$. From the LDA analysis this error was estimated to be $0 < \delta(e_V) < 5\%$. If the processing error at any grid point is represented by the percentage error $\delta(U_P)$, then the total percentage error in PIV velocity measurement, $\delta(U_{\mathrm{PIV}})$ can be found from

$$\delta(U_{\mathrm{PIV}}) = \sqrt{[\delta(U_P)]^2 + [\delta(e_V)]^2}. \tag{A1}$$

The processing error originates from a calibrated magnification M, the estimate of particle image displacement Δs and the pulse separation Δt such that if the uncertainty in measurement of the quantities M, Δs and Δt is represented by the percentage errors $\delta(M)$, $\delta(\Delta s)$ and $\delta(\Delta t)$, respectively, then the total processing error in velocity measurement, $\delta(U_P)$ can be found from

$$\delta(U_P) = \sqrt{[\delta(M)]^2 + [\delta(\Delta s)]^2 + [\delta(\Delta t)]^2}. \tag{A2}$$

The magnification M was estimated from an image of a ruler placed in the light sheet plane prior to the PIV measurements where the error was typically 1 pixel in 500 or $\delta(M) = 0{\cdot}2\%$. For the pulse separation an estimate of Δt was taken from a oscilloscope readout of a fast photodiode placed adjacent to the laser output beam. Typical errors were 1 pixel in 200 or $\delta(\Delta t) = 0{\cdot}5\%$. The error in particle image displacement, $\delta(\Delta s)$, can be found from previous

analysis of the cross-correlation function by Keane & Adrian (1992). This error is strongly dependent on the spatial velocity gradient and for our measurements was estimated to be a maximum of 0·5% of full-scale velocity in the region adjacent to the nozzle exit. This results in an expected full-scale velocity error of 0·73%. This full-scale error will correspond to a processing error range of $2{\cdot}5\% < \delta(U_P) < 7{\cdot}3\%$ if the particle displacement is validated across 10–30% of the grid spacing where the greater error occurs at the lower velocities (Keane & Adrian 1992). Finally, if an error due to the seeding response is included, the total velocity measurement error would be expected to lie in the range of $2{\cdot}5 < \delta(U_{\mathrm{PIV}}) < 8{\cdot}9\%$.